ARTICLE

Check for updates

Room temperature all-solid-state lithium batteries based on a soluble organic cage ionic conductor

Jing Li[1,2,3], Jizhen Qi[2], Feng Jin[2], Fengrui Zhang[2], Lei Zheng[2], Lingfei Tang[2], Rong Huang[4], Jingjing Xu[2], Hongwei Chen [5], Ming Liu [6], Yejun Qiu [1✉], Andrew I. Cooper [6✉], Yanbin Shen [2✉] & Liwei Chen [2,4,7✉]

All solid-state lithium batteries (SSLBs) are poised to have higher energy density and better safety than current liquid-based Li-ion batteries, but a central requirement is effective ionic conduction pathways throughout the entire cell. Here we develop a catholyte based on an emerging class of porous materials, porous organic cages (POCs). A key feature of these Li$^+$ conducting POCs is their solution-processability. They can be dissolved in a cathode slurry, which allows the fabrication of solid-state cathodes using the conventional slurry coating method. These Li$^+$ conducting cages recrystallize and grow on the surface of the cathode particles during the coating process and are therefore dispersed uniformly in the slurry-coated cathodes to form a highly effective ion-conducting network. This catholyte is shown to be compatible with cathode active materials such as $LiFePO_4$, $LiCoO_2$ and $LiNi_{0.5}$-$Co_{0.2}Mn_{0.3}O_2$, and results in SSLBs with decent electrochemical performance at room temperature.

[1] Shenzhen Engineering Lab of Flexible Transparent Conductive Films, School of Materials Science and Engineering, Harbin Institute of Technology, Shenzhen 518055, China. [2] i-Lab, CAS Center for Excellence in Nanoscience, Suzhou Institute of Nano-Tech and Nano-Bionics (SINANO), Chinese Academy of Sciences, Suzhou 215123, China. [3] School of Materials Science and Engineering, Suzhou University of Science and Technology, Suzhou 215009, China. [4] Vacuum Interconnected Nanotech Workstation (Nano-X), Suzhou Institute of Nano-Tech and Nano-Bionics, Chinese Academy of Sciences, Suzhou 215123, China. [5] College of Materials Science and Engineering, Huaqiao University, Xiamen 361021, China. [6] Leverhulme Centre for Functional Materials Design, Materials Innovation Factory and Department of Chemistry, University of Liverpool, Liverpool L697ZDUK. [7] In-situ Center for Physical Sciences, School of Chemistry and Chemical Engineering, Shanghai Jiaotong University, Shanghai 200240, China. ✉email: yejunqiu@hit.edu.cn; aicooper@liverpool.ac.uk; ybshen2017@sinano.ac.cn; lwchen2008@sinano.ac.cn

Solid-state lithium (Li) batteries have theoretically higher energy densities and better safety characteristics than organic solvent-based Li-ion batteries[1,2]. Research in the solid-state battery field has focused mostly on developing solid-state electrolytes (SSEs)[3–6] and improving their interfaces with the cathode and anode[7–9]. This has yielded various promising SSEs with bulk Li$^+$ ion conductivity in the 10^{-6}–10^{-3} S cm^{-1} range and various technical solutions have been developed to address the solid electrode/electrolyte interfacial problem[10–13]. A critical but less addressed problem, however, lies in the Li$^+$ ion transport in solid-state cathodes, especially when thick cathodes with practically meaningful areal loadings are considered[14,15].

So far, there are three main strategies to construct the Li$^+$ transport networks inside solid-state cathodes. The first approach is to add a defined amount of liquid electrolyte, ionic liquid, or plastic crystal with a Li salt to a porous cathode structure[16–19]; for example, 50~100 µL plastic crystal electrolyte[16] or 20% succinonitrile/LiTFSI[19] were added to solid-state cathodes to obtain good ionic conductivity. However, for high energy density batteries with high capacity and high voltage electrode materials, such as metallic Li anode, Ni-rich layered cathode, and lithium nickel manganese spinel cathodes, most of the commonly used organic electrolytes tend to decompose due to their narrow electrochemical windows and form SEI or CEI, causing the cell capacity to "rollover" when the liquid in the electrode is depleted after repeated cycles. As such, removing all liquid components to realize all-solid-state batteries with high safety and high energy density is the ultimate goal. A second approach is to introduce inorganic SSEs as catholytes, such as Li$_7$La$_3$Zr$_2$O$_{12}$ (LLZO) and Li$_{10}$GeP$_2$S$_{12}$ (LGPS), in solid-state cathodes[20,21]. Inorganic SSEs are insoluble and can only be added in the form of particles, which are prone to aggregation and poor dispersion in the cathodes. Hence, to ensure effective ion transport in the cathodes, a large amount of the inorganic SSEs is often needed in the cathode mixture, typically 20–60 wt%, which inevitably lowers the energy density. Moreover, poor solid-solid contact between the ceramic SSE particles and active material can result in high energy barrier for Li ion transport[22,23]. A third approach is to add polymer electrolytes with Li salts to facilitate ion transport. However, most polymer electrolytes still face problems of having a narrow electrochemical window and low ion conductivity at room temperature[24–26]. As a result of these various limitations, few reports on room temperature SSLB have displayed satisfactory electrochemical performance for future practical applications[27]. For example, high amounts (30–60%) of SSE are often needed in solid-state cathodes[20,21,28], and complicated preparation procedures may be required[29] to construct solid-state cathodes, sometimes resulting in only limited cycle life[30]. As such, the construction of efficient Li$^+$ transport networks in stable solid-state cathodes are important and urgent if we are to build SSLBs with satisfactory performance at room temperature.

Here we report the use of a soluble organic cage-based Li$^+$ conductor as catholyte for room temperature SSLBs. Porous solids, such as metal–organic frameworks (MOFs)[31,32] and covalent organic frameworks (COFs)[33–35], have been explored extensively for their ion conduction properties. Unlike MOFs and COFs, which are extended, insoluble frameworks, organic cages have discrete molecular covalent structures, and can be solution processable[36]. Such molecules can pack together to form crystals with highly interconnected three-dimensional pore networks. The discrete nature of cage molecules renders them soluble in different solvents[37], which offers processability and can introduce different physical properties by mixing with other soluble compounds[38–40]. For example, a series of crystalline porous amine cages was developed for proton conduction, and the resulting proton conductivities were comparable with

MOFs[41]. However, to date, there have been no Li ion conductors based on porous organic cages.

In the organic cage-based solid-state Li$^+$ conductor developed in this work, ionized functional groups in the organic cage framework provide an environment with high effective dielectric screening, thus allowing an added Li salt, such as LiClO$_4$, to dissociate into mobile ions. In addition to exhibiting highly desirable room temperature ionic conductivity, a key feature of this organic cage-based ion conductor is its solubility in polar solvents. Hence, the organic cage Li$^+$ conductor is readily incorporated into solid-state cathodes as a catholyte in the slurry mixing step. The cage catholyte, which is dissolved uniformly in the cathode slurry, crystallizes upon solvent evaporation and grows on the surface of the cathode particles during the coating process, thus forming an effective ion conduction network inside the cathode. This approach of using organic cages in SSLBs can minimize the quantity of ionic additive needed for the cathode and leads to excellent room temperature cycling performance.

Results and discussion

Synthesis and characterization of Li-RCC1-ClO$_4$. As shown in Fig. 1a, the SSE was derived from a three-dimensional porous organic cage, RCC1-Cl, which comprises of a cationic amine cage framework (RCC1) and chloride counterions, as used previously as a proton conductor[41,42]. Here, the chloride counterions in RCC1-Cl were exchanged with perchlorate ions, resulting in a different cage, RCC1-ClO$_4$, which was then blended with LiClO$_4$ salt to form a SSE, Li-RCC1-ClO$_4$.

Scanning electron microscope (SEM) images (Supplementary Fig. 1), X-ray diffraction (XRD) patterns (Supplementary Fig. 2) and nuclear magnetic resonance (NMR) spectra (Supplementary Fig. 3) collected for the RCC1-Cl sample are consistent with previous reports[42]. The SEM image in Fig. 1b shows that submicron-sized particles of the Li-RCC1-ClO$_4$ material crystallize from an ethanol/water solvent mixture (v:v = 3:1) and these are interconnected with each other to form a fluffy aggregate. The energy-dispersive X-ray spectroscopy (EDX) measurement of the prepared Li-RCC1-ClO$_4$ solid pellet presented in Supplementary Fig. 4 shows that the LiClO$_4$ is dispersed uniformly in the solid. X-ray photoelectron spectroscopy (XPS) was used to monitor the formation of the Li-RCC1-ClO$_4$ SSE. As shown in Fig. 1c, the RCC1-Cl sample shows the pair of characteristic Cl 2p peaks at 200.0 and 198.4 eV, indicating the bonding of the chloride ions to the RCC1 cage[43,44]; while the Cl 2p peaks obtained from the RCC1-ClO$_4$ sample appears at 209.7 and 208.2 eV, which is slightly lower in binding energy than that of LiClO$_4$ salt (211.0 and 209.4 eV)[45], indicating that the chloride ions have been exchanged to perchlorate ions and the perchlorate ions are weakly coordinated to the -NH$_2^+$- groups on the cage skeleton. After adding LiClO$_4$ salt to the RCC1-ClO$_4$, two distinct sets of Cl 2p peaks can be observed. One set of the Cl 2p peaks is found at 209.8 eV and 208.3 eV (Fig. 1d), which is similar to peaks observed for weakly-coordinated perchlorate ions (Fig. 1c); another set of Cl 2p peaks appears at lower binding energies of 207.8 eV and 206.2 eV, which might be attributed to free perchlorate ions that dissociated from the added LiClO$_4$ salt (the molar ratio of [Li$^+$]/[-NH$_2^+$-] is ~1:1; the influence of the salt concentration on the Li-RCC1-ClO$_4$ SSE is discussed in later sections).

The existence of perchlorate ions in different chemical environments was also observed in Raman spectra. As shown in Fig. 1e, the LiClO$_4$ reference sample shows a characteristic sharp peak at ~937 cm^{-1}, which can be assigned to the Li$^+$/ClO$_4^-$ ion pairs, while both the RCC1-ClO$_4$ and Li-RCC1-ClO$_4$ samples exhibit characteristic peaks at a lower wavelength (~935 cm^{-1} and ~932 cm^{-1}, respectively) that can be assigned for weakly
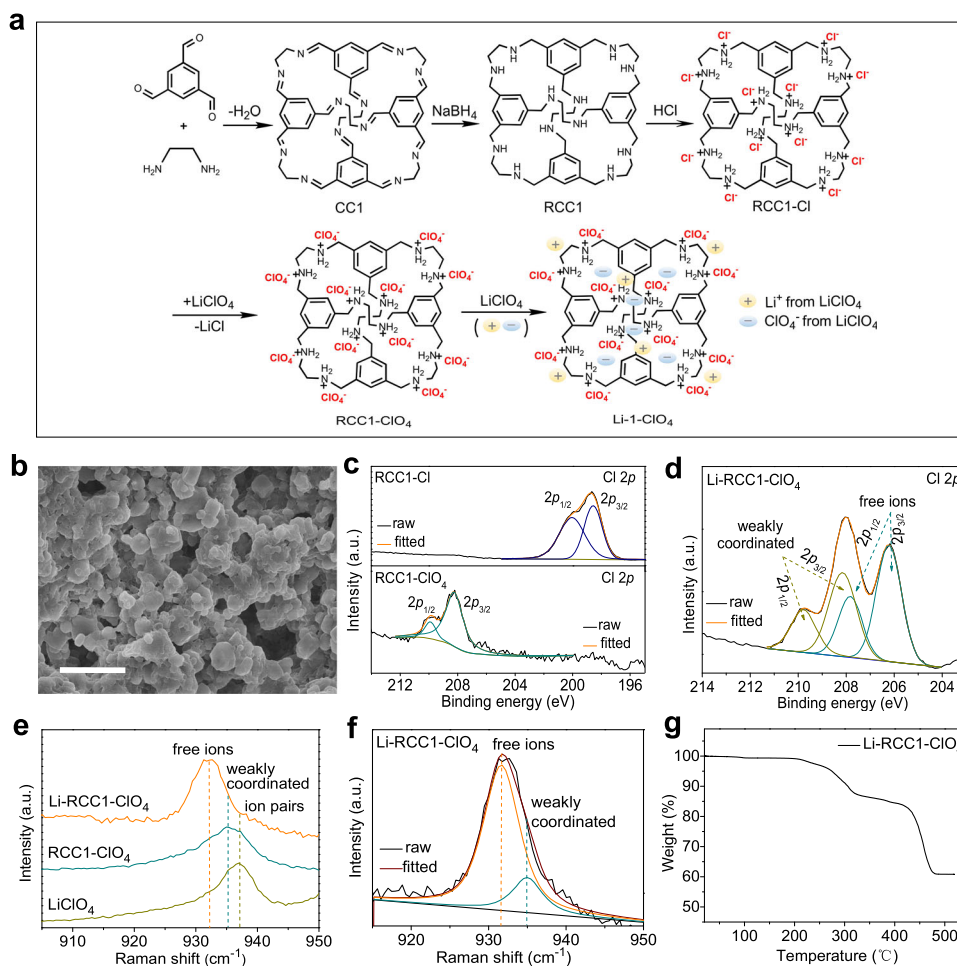
Fig. 1 Synthesis and characterization of the cage-based SSE, Li-RCC1-ClO₄. a Synthetic procedure for the porous cage electrolyte Li-RCC1-ClO₄. Note: the light yellow and blue symbol represent Li ion and ClO₄ ion from LiClO₄, respectively. **b** SEM micrograph of Li-RCC1-ClO₄ powder. **c**, **d** XPS Cl $2p$ spectra of RCC1-Cl, RCC1-ClO₄, and Li-RCC1-ClO₄. **e** Raman spectra of LiClO₄, RCC1-ClO₄ and Li-RCC1-ClO₄. **f** Fitting of the Li-RCC1-ClO₄ Raman spectrum in the range of 915-950 cm^{-1}. **g** Thermogravimetric analysis for Li-RCC1-ClO₄ under N₂ atmosphere (heating rate: 10 °C/min). Scale bar for **b** is 5 μm.

coordinated and free perchlorate ions[46–48]. Based on the integrated peak areas, it can be estimated that the free and weakly coordinated perchlorate ions in the Li-RCC1-ClO₄ SSE are about 82% and 18%, respectively (Fig. 1f), assuming that the extinction coefficients for the Raman peaks are comparable. The perchlorate ions in the Li-RCC1-ClO₄ SSE are therefore either weakly coordinated to the RCC1 cage skeleton or in a "free" form; this suggests that the Li$^+$ in the LiClO₄ salt should be well dissociated from the anions, which is beneficial for ionic conductivity. The Li-RCC1-ClO₄ SSE also has a good thermal stability: it only starts decomposing at temperatures higher than 220 °C (Fig. 1g). By contrast, many polymer electrolytes, such as PEG-based materials, will decompose at temperature below 200 °C[49,50].

Electrochemical performance of Li-RCC1-ClO₄. The ionic conductivity of the Li-RCC1-ClO₄ SSE is sensitive to the molar ratio of [Li$^+$]/[-NH₂$^+$-]. As calculated based on the resistance obtained from electrochemical impedance spectroscopy (EIS) measurements (Fig. 2a and Supplementary Fig. 5), the room temperature ion conductivity of the Li-RCC1-ClO₄ SSE increases as the content of the LiClO₄ increases, and reaches a peak value of 5.13×10^{-5} S cm^{-1} at a molar ratio [Li$^+$]/[-NH₂$^+$-] of about 1. Further increase in the content of the Li salt to a molar ratio of [Li$^+$]/[-NH₂$^+$-] greater than 1:1 will result in an increase in residual undissociated LiClO₄ (Supplementary Fig. 6), leading to

decreased ion conductivity. Supplementary Fig. 7 and Fig. 2b show the ionic conductivity of the Li-RCC1-ClO₄ SSE at different temperatures, which reaches 1.2×10^{-4} S cm^{-1} at 60 °C; the activation energy is calculated to be 0.34 eV. This room temperature conductivity is considerably higher than some polymer SSEs, such as PEO and PVDF SSEs[51,52]. More importantly, the Li-RCC1-ClO₄ SSE show a wide electrochemical window up to 5.0 V (Fig. 2c) and a very high ion transference number of ~0.7 is obtained for the Li-RCC1-ClO₄ SSE (Fig. 2d and Supplementary Fig. 8), confirming the disassociation of LiClO₄ and suggesting that the -NH₂$^+$- groups in the cage molecule restrict movement of the ClO₄$^-$ anions.

This is the first report of a porous organic material that can be used as Li ion solid-state electrolyte without any solvent. It has a room temperature ionic conductivity of 5.13×10^{-5} S cm^{-1}, an electrochemical window up to 5.0 V, and a transfer number of ~0.7. More importantly, the discrete molecular structure of the cage makes it soluble in common polar solvents, and thus can be facilely mixed with electrode materials by slurry-coating, an industrial compatible electrode preparation process. As such, this cage-containing electrolyte is advantageous for constructing ionic conducting pathways inside solid-state cathodes.

Application of Li-RCC1-ClO₄ in all-solid-state cathodes. Li-RCC1-ClO₄ has potential as an SSE because it exhibits an ionic
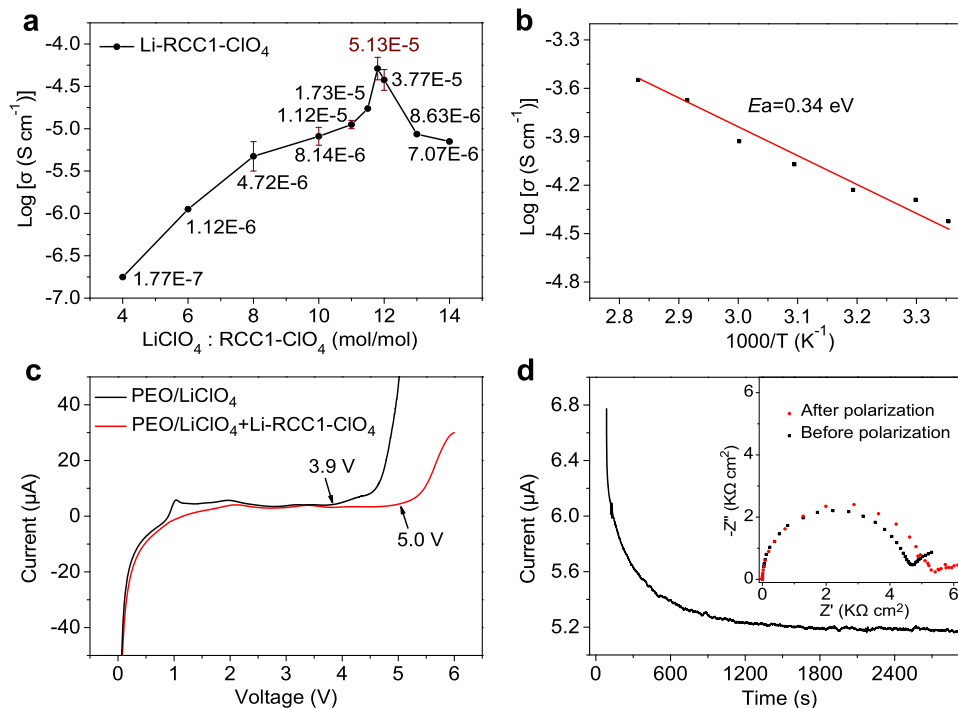
Fig. 2 Electrochemical characterization of Li-RCC1-ClO₄. **a** Ion conductivity of the Li-RCC1-ClO₄ SSE with different LiClO₄ contents. **b** Ion conductivity of Li-RCC1-ClO₄ as a function of temperature. **c** Linear sweep voltammetry (LSV) results of PEO/LiClO₄ and PEO/Li-RCC1-ClO₄ at a scan rate of $1 \, \text{mV s}^{-1}$. **d** Time-dependent current before and after direct-current (DC) polarization (with a DC voltage of 50 mV). The insert image shows the EIS results of Li-RCC1-ClO₄ symmetric cell before and after polarization.

conductivity of $5.13 \times 10^{-5} \, \text{S cm}^{-1}$ at room temperature, which is comparable to the best-performing polymer SSEs reported[53,54]. It is particularly promising for all-solid-state cathodes because of its processing advantages. Unlike insoluble network polymers and extended frameworks, such as MOFs and COFs, this porous organic cage can be dissolved in a variety of solvents, such as water and methanol ($10 \, \text{mg mL}^{-1}$, Fig. 3a), offering a range of solution-processing options. Here, the ion-conducting organic cage Li-RCC1-ClO₄ was used to address the ion conduction issue in solid-state cathodes. The solution processability of the organic cage allows the problem to be tackled with the conventional slurry coating method, which is the process used in the manufacturing of current liquid electrolyte batteries. The solid-state cathode contained LiFePO₄ as the active material, acetylene black (AB) and carbon nanotubes (CNTs) as electronic conductors, polyvinylidene fluoride (PVDF) as a binder, and Li-RCC1-ClO₄ as the ionic conductor, combined in the weight ratio LiFePO₄:AB:CNTs:PVDF:Li-RCC1-ClO₄ = 71:4:2:3:20 (that is, 20 wt.% of the organic SSE). Methanol/N-methylpyrrolidone (NMP) was used as the solvent (Supplementary Fig. 9).

As shown in Supplementary Fig. 10 and Fig. 3b, the LiFePO₄ particles in the resulting solid-state cathode are interconnected by a binder-like substance, which was identified by elemental mapping of EDX to be the Li-RCC1-ClO₄ SSE. As shown in Fig. 3c–e, the Fe signal from LiFePO₄ shows a clear particle shape (Fig. 3c); on the other hand, the N and Cl signals arise from the Li-RCC1-ClO₄ (Fig. 3d, e) are distributed throughout the field of view, surrounding these LiFePO₄ particles. These observations suggest that Li-RCC1-ClO₄ crystallizes from the NMP/methyl alcohol mixture and forms an ionic conducting network surrounding and interconnecting the LiFePO₄ particles. In sharp contrast, a cathode prepared using the same method but without Li-RCC1-ClO₄ was discontinuous and most of the LiFePO₄ particles were isolated from each other (Supplementary Fig. 11a–c). EDX mapping for this cathode (Supplementary

Fig. 11d–h) also showed a clear particle-shaped Fe signal but negligible signals from N and Cl. Similar results were observed in the depth direction of the cathode using cross sectioned samples prepared by focus-ion-beam (FIB) milling. As shown in Fig. 3f, g, SEM images for cathode cross sections show that most LiFePO₄ particles are isolated from each other without the Li-RCC1-ClO₄ additive (Fig. 3f), while the LiFePO₄ particles in the cathode with the Li-RCC1-ClO₄ SSE are interconnected by the ion conductor (Fig. 3g).

Time-of-flight secondary ion mass spectrometry (TOF-SIMS) was also used to assay the distribution of the catholytes inside the cathode. Figure 3h, i show the 3D chemical images and depth profiling of the cathode with Li-RCC1-ClO₄, in which the PO_3^-, CN^- (and ClO_3^-) fragments can be attributed to the LiFePO₄ and Li-RCC1-ClO₄, respectively. As shown in Fig. 3h, the PO_3^- fragments occupy most of measured volume, while the CN^- and ClO_3^- fragments fill the remaining space. The corresponding normalized depth profile in Fig. 3i also reveals that the distribution of the PO_3^-, CN^- (and ClO_3^-) fragments through the cathode are complementary, confirming that the LiFePO₄ particles are surrounded homogeneously by the Li-RCC1-ClO₄ catholyte.

Fourier transform infrared (FTIR) spectra (Fig. 3j) showed that the characteristic absorption peaks of Li-RCC1-ClO₄ SSE are unchanged in the LiFePO₄ solid-state cathode, indicating stability of the cage catholyte. The powder X-ray diffraction (PXRD) pattern (Fig. 3k) shows that the characteristic diffraction peak (marked with asterisk) of Li-RCC1-ClO₄ is retained, suggests that the crystal structure of Li-RCC1-ClO₄ is also preserved. However, there is an obvious loss of crystallinity in the slurry-coated solid cathode in comparison to Li-RCC1-ClO₄ in its pure powder form. We speculate that the interactions between LiFePO₄ and the Li-RCC1-ClO₄ SSE, likely the ionic interactions between NH_2^+ on cages and PO_4^- from LiFePO₄, may affect the recrystallization of the cage in slurry coating and also allow Li-RCC1-ClO₄ to grow into a thin layer on the surface of the LiFePO₄ particles, rather
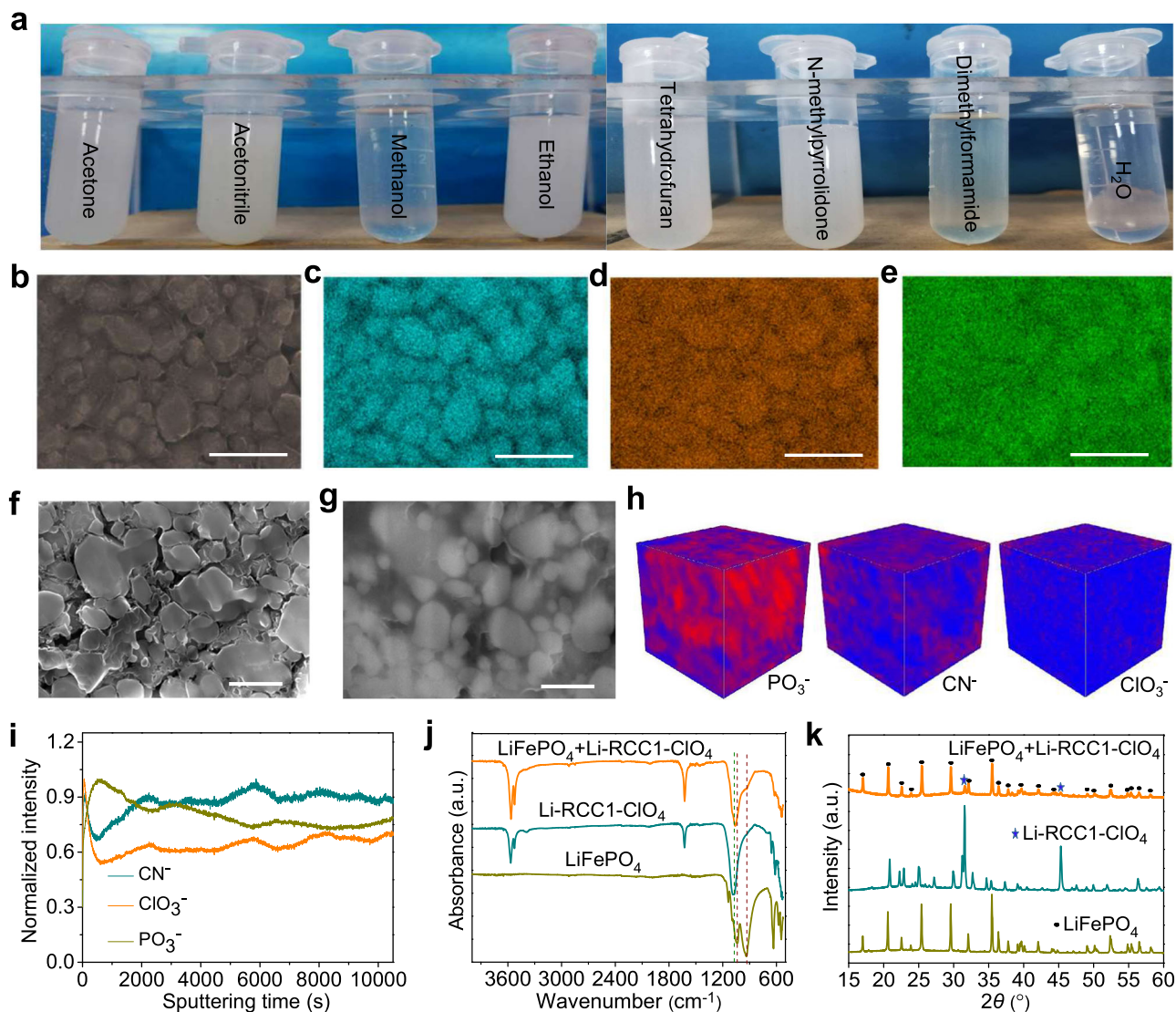
Fig. 3 Characterization of Li-RCC1-ClO₄ in all-solid-state cathodes. a Solubility of Li-RCC1-ClO₄ in different solvents. **b** SEM image and **c–e** EDS elemental mappings of Fe, N and Cl in the cathode with Li-RCC1-ClO₄. SEM micrographs of focus-ion beam cut cross-section of the solid cathodes without (**f**) and with Li-RCC1-ClO₄ (**g**). **h** TOF-SIMS 3D renderings of the solid cathode with Li-RCC1-ClO₄. **i** Normalized TOF-SIMS depth profiles of the solid cathode with Li-RCC1-ClO₄. **j** FTIR spectra of LiFePO₄, Li-RCC1-LiClO₄ and mixture of LiFePO₄ and Li-RCC1-ClO₄. **k** XRD patterns of LiFePO₄, Li-RCC1-LiClO₄ and mixture of LiFePO₄ and Li-RCC1-ClO₄. Scale bars for **b–g** are all 500 nm.

than crystallize into a large crystalline particle during the slurry coating process; this could in turn affect the relative intensity of the PXRD peaks due to preferred orientation. This morphology change, however, also results in more efficient utilization of the cage catholyte with respect to insoluble particulate SSEs, and we believe that helps to create continuous ionic conducting pathways and to reduce interfacial resistance by using a relatively small dose of the additive.

Electrochemical performance of all-solid-state batteries with Li-RCC1-ClO₄ as catholyte. The Li-RCC1-ClO₄ catholyte in the LiFePO₄ solid-state cathode was optimized by comparing the specific capacity and polarization of the SSLB. For solid-state cathodes with 0, 10, 20 and 30 wt% Li-RCC1-ClO₄ additive (Supplementary Fig. 12), the specific capacity increases and the polarization decreases as the Li-RCC1-ClO₄ content increases from 0 wt% to 20 wt%. The performance then deteriorates when the amount of Li-RCC1-ClO₄ is increased further to 30 wt%.

Higher Li-RCC1-ClO₄ contents results in increased polarization, probably because the electronic conducting pathway is negatively affected by the ionic conducting additive. The optimized additive content was therefore set to be 20 wt%, which is significantly less than the more typical values of 30–60 wt% for inorganic SSE additives[28,29,55]. Furthermore, the ionic conductivities of the solid cathodes with different Li-RCC1-ClO₄ content and LiFePO₄ areal loading were investigated systematically. As shown in Fig. 4a and Supplementary Table 1, when the content of Li-RCC1-ClO₄ was higher than 20%, the ionic conductivities of solid-state cathodes with 1, 2, 3, 4, 5, 6 mg cm⁻² of active materials were similar, indicating that Li-RCC1-ClO₄ could construct effective ionic conductivity network in thick solid-state cathode. The average ionic conductivity of the cathode with 20% and 30% Li-RCC1-ClO₄ was 4.64×10^{-5} and 5.06×10^{-5} S cm⁻¹, respectively. Even though the latter has a slightly higher conductivity, 20% of Li-RCC1-ClO₄ catholyte was still the best choice when taking energy density and electronic conductivity into consideration (too much electrolyte might hinder the electron conduction).
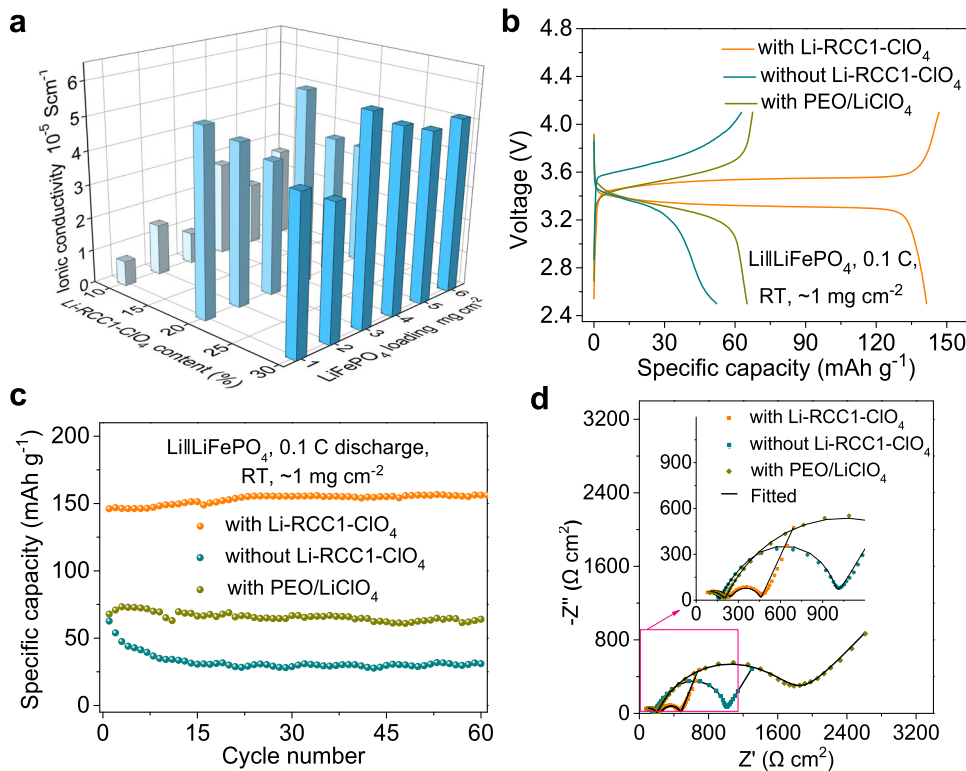
Fig. 4 Electrochemical performance of the all-solid-state battery with ionic conducting cage catholyte Li-RCC1-ClO$_4$. a Comparison of the ionic conductivities of the solid cathodes with different Li-RCC1-ClO$_4$ content and LiFePO$_4$ areal loading. Note: the cyan from light to dark symbol represent solid-state cathode with 10%, 20% and 30% Li-RCC1-ClO$_4$ electrolyte, respectively; The detailed values are provided in Supplementary Table 1. **b** Voltage profiles, **c** cycling performance, and **d** Electrochemical impedance spectra profiles of the SSLBs at room temperature using LiFePO$_4$ solid-state cathodes (loading: ~1.0 mg cm^{-2}) with and without Li-RCC1-ClO$_4$, as well as with PEO/LiClO$_4$ polymer as the catholyte. The inset in 4d shows the enlarged impedance curves of the red square. The fitted modal is shown in Supplementary Fig. 15.

The LiFePO$_4$ solid-state cathode (with a weight ratio of LiFePO$_4$:AB:CNTs:PVDF: Li-RCC1-ClO$_4$ = 71:4:2:3:20) was then assembled with a lithium foil anode and a polymer solid electrolyte, P(IL-PEGDA), which was dried and stored in glove box for one week to remove residual solvent, as reported in our previous work[56], to form a coin cell SSLB. This could be used to light an LED (Supplementary Fig. 13). Figure 4b, c compares the electrochemical performance of coin cells using LiFePO$_4$ solid-state cathodes (loading: ~1.0 mg cm^{-2}) with and without the Li-RCC1-ClO$_4$ catholyte, as measured at room temperature. To compare with commonly used polymer ion conductors, we also evaluated the performance of LiFePO$_4$ solid-state cathode containing PEO/LiClO$_4$ as the catholyte instead of the Li-RCC1-ClO$_4$. As shown in Fig. 4b, the cell with Li-RCC1-ClO$_4$ catholyte exhibits discharge and charge profile with a voltage plateau at ~3.4 V and an initial specific capacity of ~147 mAh g^{-1} at 0.1 C, similar to a LiFePO$_4$ cell with liquid electrolyte[57]. By contrast, very large polarization and limited initial specific capacity was observed from cells without Li-RCC1-ClO$_4$ (~530 mV, 52 mAh g^{-1}) or with the PEO/LiClO$_4$ catholyte (~700 mV, 65 mAh g^{-1}). Without the Li-RCC1-ClO$_4$ catholyte, or with the PEO/LiClO$_4$ catholyte, much of the LiFePO$_4$ material in the cells is unutilized, or underutilized, because of the absence a sufficient ionic conducting network in the solid-state cathodes[58]. Their corresponding cycling performance and coulombic efficiency is shown in Fig. 4c and Supplementary Fig. 14, respectively. The SSLB cells containing the Li-RCC1-ClO$_4$ catholyte delivers an initial discharge capacity of 147 mAh g^{-1} and can run stably with capacity of 152 mAh g^{-1} at 0.1 C with stable coulombic efficiency nearly 100%; while the battery without

Li-RCC1-ClO$_4$ additive or with PEO/LiClO$_4$ as catholyte presents extremely low capacity and floating coulombic efficiency almost between 95–100%. These are consistent with EIS results, shown in Fig. 4d, which reveal that the total impedance of the SSLB with the Li-RCC1-ClO$_4$ catholyte is ~468 Ω cm^2; that is, much lower than the 992 Ω cm^2 measured for the battery without Li-RCC1-ClO$_4$ and the 1737 Ω cm^2 measured for the battery containing PEO/LiClO$_4$. The Nyquist plots of the Li‖LiFePO$_4$ cells with different catholytes show two semicircles (Fig. 4d). To construct the equivalent circuit for the EIS data, Li|SSE|Li and SS|SSE|SS symmetry cells were assembled and investigated (Supplementary Fig. 15) to help identifying each part of the resistance in the Li‖LiFePO$_4$ cell shown in Fig. 4d. As shown in Supplementary Fig. 15a, the semicircle (~100 Ω cm^2) for the SS|SSE|SS cell at high frequency (>1.5 MHz) is assigned to the resistance of solid-state electrolyte, and the semicircle (~220 Ω cm^2) for the Li|SSE|Li cell at middle and low frequency (the apex value of the semicircle is 2.2 KHz) is attributed to the Li|SSE interfacial charge transfer resistance. And the semicircle at the low frequency (the apex value of the semicircle is 320 Hz) should be attributed to the cathode|SSE interfacial charge transfer resistance[19,29]. Based on these results, equivalent circuit used for fitting the EIS of three different Li‖LiFePO$_4$ cells is obtained (Supplementary Fig. 15b). A summary of the fitting results is given in Supplementary Table 2. In which all of the fitting results of X^2 are close to 10^{-3}, indicating a good fitting of the EIS data. With the Li-RCC1-ClO$_4$ additive, the cathode|SSE interface showed a relatively low resistance of ~255 Ω cm^2 at RT, which is much smaller than 785 and 1520 Ω cm^2 for the cell without Li-RCC1-ClO$_4$ and with PEO/LiClO$_4$ catholyte, respectively, suggesting the successful

construction of effective ion conducting pathway in the cathode by Li-RCC1-ClO$_4$ catholyte.

We also evaluated the LiFePO$_4$ solid-state cathode at higher charge/discharge rates and at higher cathode loadings, since these are important parameters that govern the cell power density and energy density of the SSLB. When the current of the 1.0 mg cm^{-2} LiFePO$_4$ solid-state cathode was increased to 0.5 C, it showed a specific capacity of 122~135 mAh g^{-1} during 200 cycles at room temperature (Supplementary Fig. 16a). The initial coulombic efficiency of the ASSLMB is 93.4%, which subsequently increases to 99.9% and 100.0% in the second and third cycle, and maintained nearly 100% in the following 200 cycles at 0.5 C (Supplementary Fig. 16b). Its corresponding voltage-capacity curves were shown in Supplementary Fig. 17. This result suggests that the contact between the electrode material and the electrolyte is good during charge and discharge. Further increased the current to 1.0 C, the LiFePO$_4$ SSLB shows even better cycle stability, with 88.2% capacity retention at the 750th cycle, corresponding to 0.026% capacity decay per cycle (Fig. 5a and Supplementary Fig. 18). The morphology of the LiFePO$_4$ cathode after 750 cycles was investigated by SEM. As shown in Supplementary Fig. 19, there was no obvious changes, such as cracks or deformation, in the cycled LiFePO$_4$ cathode when compared with the LiFePO$_4$ cathode before cycling (Supplementary Fig. 10), demonstrating the Li-RCC1-ClO$_4$ catholyte can maintain the morphology of the solid cathode during charge-discharge processes.

Ion-conduction in thick solid cathode will be more challenging. As shown in Fig. 5b and Supplementary Fig. 20, there were no obvious difference in the 0.1 C cycle life of the all-solid-state batteries with different LiFePO$_4$ areal loadings of 2, 3 and 4 mg cm^{-2}. However, rate performance of the batteries differed by areal loading (Fig. 5c). The discharge capacity of the battery with a thicker cathode declines faster as the current density increases. This may be attributed to the coarse and fluffy deposited Li at high areal capacity, which result in poor solid-solid contact between the Li metal anode and solid electrolyte[59,60]. Thus, the surface morphology of the lithium anodes before and after cycled at different current densities were further investigated, as shown in Supplementary Fig. 21. The lithium foil presented was observed to become coarse and fluffy as the LiFePO$_4$ areal loading increased from 2 to 4 mg cm^{-2}, indicating that the lithium anode side is problematic with high areal capacity.

As shown in Supplementary Fig. 22a, when the rate of the 2 mg cm^{-2} LiFePO$_4$ solid-state cathode was increased from 0.1 to 0.5 C at room temperature, it still delivered an initial specific capacity of ~90 mAh g^{-1}, which slowly increased to ~115 mAh g^{-1} in subsequent cycles. When both the C-rate and temperature were increased at the same time to 0.5 C and 60 °C, the 2 mg cm^{-2} LiFePO$_4$ solid-state cathode showed a discharge capacity of ~135 mAh g^{-1} with a relatively stable cycle life, which was close to that obtained at 0.1 C at room temperature (Supplementary Fig. 22b).

The capacity and cycle stability of the cell with the Li-RCC1-ClO$_4$ catholyte at 60 °C was much better than that for the PEO/LiClO$_4$ catholyte, which exhibited a specific capacity of ~90 mAh g^{-1} and a capacity retention of 75.6% after 50 cycles (Supplementary Fig. 23). Additional cycling results for the Li-RCC1-ClO$_4$ containing cells with different cathode loadings are provided in Supplementary Fig. 24. This SSLB performance is among the best reported in the literature (Supplementary Fig. 25 and Supplementary Table 3)[21,61–67], particularly in terms of the room-temperature performance and long-term cycling performance.

To check whether the polymerized electrolyte layer has any contribution to the ionic conductivity of the solid-state cathode,

elemental mappings were made on the cross section of the SSLB containing the Li-RCC1-ClO$_4$ additive (cathode loading: ~1.0 mg cm^{-2}) after 50 cycles at 0.1 C/room temperature. This was mainly done to see whether the polymerized electrolyte had diffused into the cathode electrode during cycling. As shown in Supplementary Fig. 26, the characteristic elements Al of the Al foil, Fe of the LiFePO$_4$ cathode and the S of the polymerized electrolyte are observed on the current collector, the cathode, and the electrolyte layer, respectively, with a clear boundary between each. No characteristic element S of the polymerized electrolyte could be observed in the cathode layer, suggesting that no electrolyte diffused into the cathode during the cycling.

This approach is transferable to other systems: for example, this slurry coating process works not only for polymer SSEs, but is also suitable for ceramic SSEs, such as garnet-type LLZO. As shown in Supplementary Fig. 27, an Li|LLZO|LiFePO$_4$ cell with the Li-RCC1-ClO$_4$ additive showed a discharge capacity of ~130 mAh g^{-1}, while the cell without the additive hardly delivered any capacity.

This Li-RCC1-ClO$_4$ catholyte was also applied in SSLBs with high-voltage LiNi$_{0.5}$Co$_{0.3}$Mn$_{0.3}$O$_2$ (NCM523) and LiCoO$_2$ (LCO) cathodes. The solid state NCM523 cell delivers an initial discharge capacity of 165 mAh g^{-1} and an initial coulombic efficiency of 88.8% (Supplementary Fig. 28) when charged to 4.3 V. After 60 cycles, the capacity was 135 mAh g^{-1} with 81.8% retention (Fig. 5d, e). Good cycling stability of the 4.3 V and 4.4 V LCO SSLBs (Fig. 5f, g and Supplementary Fig. 29) at 0.2 C rate was also obtained, suggesting the utilization of this cage electrolyte can be extended to different types of cathodes.

In summary, we have developed an organic cage-based ionic conductor, Li-RCC1-ClO$_4$, for the preparation of high-performance solid-state cathodes. The ionic cage structure not only contributes to the high ionic conductivity and ion transference number, while also offering solution-processing options, such as the slurry coating, for cathode preparation. As such, this approach may be more broadly transferable to other kinds of SSLBs. The organic cage catholyte is dissolved in the slurry and then recrystallizes and grow on the surface of the cathode particles during the coating process, building a continuous Li ion conducting network in the solid-state cathode. As a result, the SSLBs containing 20% of this cage type SSE in the solid-state cathodes (LiFePO$_4$, NCM523, LCO) present small polarization and good cyclability at room temperature. Such molecular cage catholyte is fully compatible with current cathode manufacturing processes and have high potential for application in SSLBs. Future studies will focus on introducing additional advantages, such as better air/moisture stability and enhanced mechanical properties as well as ionic conductivity by using structured organic molecular additives such as organic cages.

Methods

Synthesis of RCC1 and RCC1-Cl. Ethylenediamine (520.0 mg, 8.65 mmol, 99.0%) was dissolved in methanol (212 mL) in a round-bottomed flask with ice bath. 1,3,5-Triformylbenzene (937.5 mg, 5.80 mmol, 98.0%) was dissolved in methanol (288 mL) and added slowly to the above ethylene diamine solution under nitrogen gas protection over 24 h. Sodium borohydride (765.0 mg, 20.15 mmol, 99.0%) was then added several times in small doses. The solution was stirred continuously during the reaction. After 12 h, 2.5 mL water was added to quench the reaction. The solvent was removed by a rotary evaporator after adding water. Subsequently, the resulting white powder was extracted with 50 mL chloroform twice. After that, the chloroform was removed under vacuum overnight and amine cage RCC1 was obtained as white powder (840 mg, ~80% yield)[42]. This was then purified using a Biotage Isolera four using a C18 reverse phase column with methanol/water as solvent. After removal of the solvent, RCC1 was obtained as a clear solid in a 42% overall yield (352 mg).

To prepare RCC1-Cl, RCC1 (500 mg, 0.612 mmol) was first added to chloroform (10 ml) with stirring. After the RCC1 had dissolved, hydrogen chloride (in dioxane, 2.3 ml, 9.18 mmol) was added dropwise to the solution. A large quantity of white precipitate appeared rapidly and the solution was stirred further
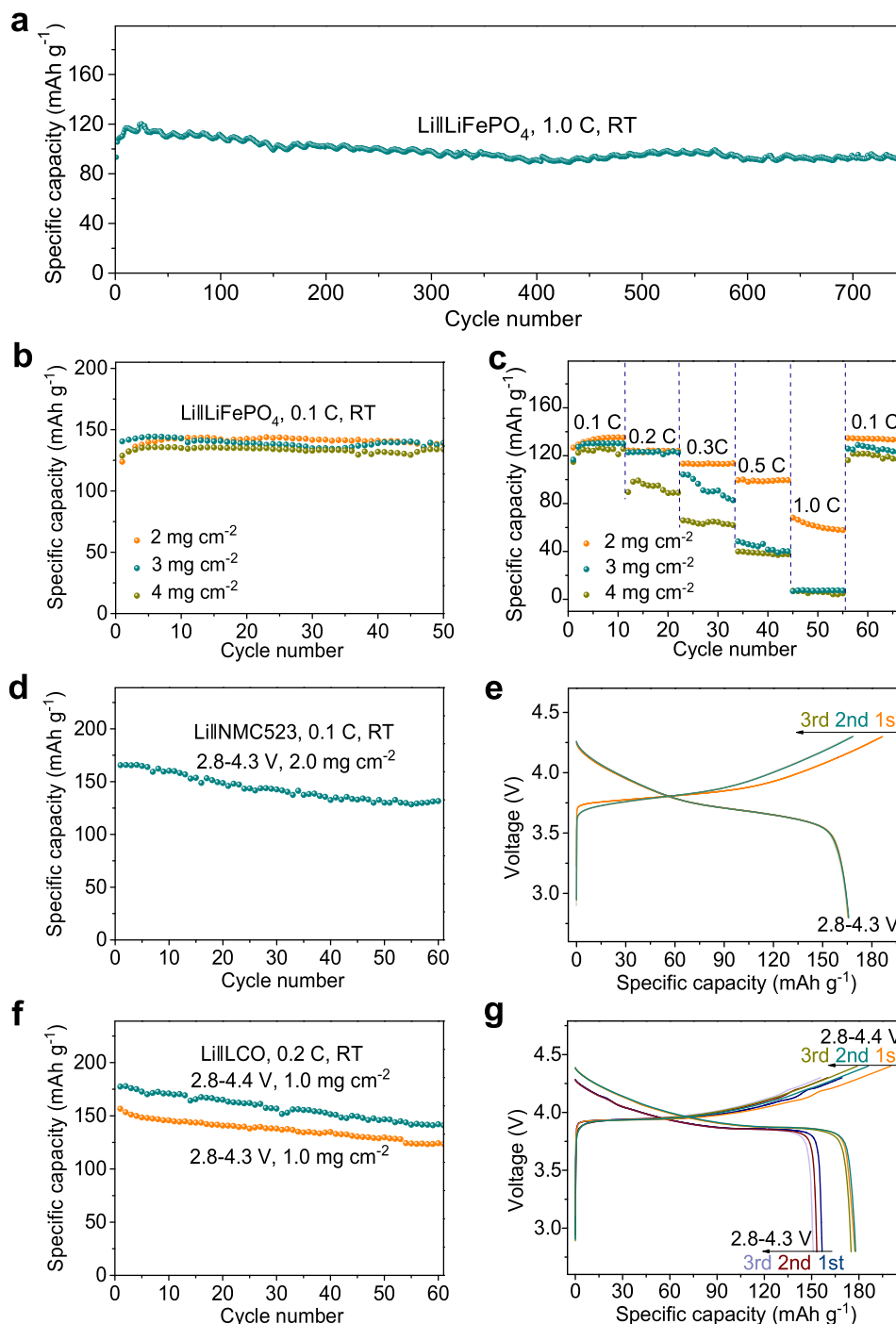
Fig. 5 Electrochemical cycling of the all-solid-state battery with Li-RCC1-ClO₄ catholyte. a Cycle performance of the all-solid-state cell with Li-RCC1-ClO₄ at 1.0 C under room temperature (loading: ~1.0 mg cm^{-2}, oscillations are due to variations in the ambient temperature). **b** Cycling performance, and **c** rate performance of the SSLBs at room temperature with different LiFePO₄ areal loading. **d** Cycle performance and **e** voltage-capacity curves of the all-solid-state cell with NCM523 cathode during 2.8~4.3 V at 0.1 C under room temperature. **f** Cycle performance and **g** voltage-capacity curves of the all-solid-state cell with LCO cathode during 2.8~4.3 V and 2.8~4.4 V at 0.2 C under room temperature.

for another 2 h. The resulting precipitate was collected by filtration then washed with chloroform (320 ml total) three times. RCC1-Cl was obtained as a white solid with a yield of 71% (532 mg) after being dried under vacuum at 90 °C[41].

Synthesis of RCC1-ClO₄ and Li-RCC1-ClO₄. The RCC1-Cl powder was dispersed in a 15 wt.% lithium perchlorate (99.0%)-ethyl acetate (100 mL, 99.9%) solution at 50 °C with stirring to allow ion exchange. The solution was changed with the fresh lithium perchlorate-ethyl acetate solution every 48 h three times. The solid product, RCC1-ClO₄, was obtained with a yield of 60% by centrifugation and washed with

ethyl acetate for three times. After ion exchange, the product was mixed with lithium perchlorate in ethanol-water solvent. The solvent was removed using a rotary evaporator. The final product, Li-RCC1-ClO₄, was collected and dried at 80 °C in vacuum overnight.

Structural characterization of Li-RCC1-ClO₄ and the all-solid-state cathode with Li-RCC1-ClO₄. Spectra for ^{1}H nuclear magnetic resonance (NMR) analysis were obtained on a Bruker Advance 400 and 600 Spectrometer in D₂O. Solution ^{1}H

NMR spectra were recorded at 300 MHz using a Bruker Avance 500 and ^{13}C NMR spectra were recorded at 75 MHz. X-ray photoelectron spectroscopy (XPS) spectra were acquired by using Thermo scientific ESCALAB 250Xi with Al Kα-radiation. All reported binding energy values are calibrated to the graphitic C 1 s peak with a value of 284.5 eV. The samples were prevented from contacting with air through a vacuum transfer device which can transfer the samples into the analysis chamber of the XPS spectrometer without exposure to the air. Fourier transform infrared (FTIR) spectra were collected using a Thermoscientific Nicolet 6700 spectrometer. Raman measurements were recorded with the laser wavelength is 532 nm. Scanning electron microscope (SEM) images were gained with a FEI Quanta 400 FEG equipped with EDX (Apollo 40 SDD) operated at 10 kV. The focus-ion-beam-milled (FIB milling) and the corresponding SEM imaging of the cross-section samples were conducted in a dual-beam Nova 200 NanoLab UHRFEG system. XRD patterns were performed on a Bruker D8-advance X-ray diffractometer with Cu-Kα radiation. Thermogravimetry (TG) curves were obtained with a Seiko 6300 thermo-gravimetric analyzer under air flow with a heating rate of 10 °C min^{-1}. Depth profiles of elemental distributions were obtained using time-of-flight secondary ion mass spectrometry (TOF-SIMS) (TOF.SIMS5-100). Bi^{+} ions at an accelerating voltage of 10 kV were used for the analysis and Cs^{+} was accelerated at 2 kV and 20 nA for sputtering. TOF-SIMS was used ex situ to probe the 3D distribution of the cathode components. For the non-in-situ tests, including FTIR, Raman, XRD, TG and TOF-SIMS, samples were placed on the sample stage and sealed in suitable stage container in an Ar-filled glovebox (O$_2$ < 10 ppm, H$_2$O < 1 ppm) until the tests begin, then open the sealed container and transfer sample stage for testing as soon as possible, and controls the ambient humidity below 20%.

Electrochemical measurements and cells assembly. Ionic conductivity of the samples was measured by electrochemical impedance spectroscopy (EIS) using an EC-lab during the frequency range from 0.01 Hz to 7 MHz with alternating current amplitude of 10 mV. Samples with Au films grown on each side with thickness of ~25 μm and diameter of 8 mm by magnetron sputtering were sandwiched in CR2032 coin cells for tests. The ionic conductivity was calculated from Eq. (1):

$$\sigma = L/(R \cdot S) \quad (1)$$

where R is the bulk resistance, L and S are the thickness and area of the solid electrolyte, respectively, in which S is calculated by the contact area between the electrolyte and Au blocking electrode.

Linear sweep voltammetry (LSV) with a sweep rate of 1 mV s^{-1} between 0 and 6.0 V, was applied on cion cells with Au working electrode as a counter and Li foil as a reference electrode on each side of the testing electrolytes. The transference number was measured and calculated by alternating current (AC) impedance and direct-current (DC) polarization (with a DC voltage of 50 mV). Li-carbon composite was coated on both side of solid-state electrolyte as non-blocking electrodes (diameter of 8 mm) to make better contact between the solid-state electrolyte and electrodes than Li foil electrodes. The Li-carbon composite slurry, including Li-CNT composite, carbon black and styrene butadiene rubber (SBR), was mixed with a mass ratio of 80:10:10 in para-xylene. After stirring for 24 h, the slurry was then coated onto both sides of the electrolyte and dried at 80 °C under vacuum overnight[68].

The Li transference number ($t_{\text{Li}+}$) was calculated as in Eq. (2):

$$t_{\text{Li}^+} = \frac{i_s\left(\Delta V - i_o R_o\right)}{i_o\left(\Delta V - i_s R_s\right)} \quad (2)$$

where I_o is the initial current, I_s is the steady-state current, ΔV is the applied potential, R_o and R_s is the overall cell resistance value before and after polarization, respectively.

The electrochemical performance of the solid-state batteries was tested with a coin cell (CR2025) assembled in an argon-filled glove box. The lithium foil (99.9%, 400 μm, Tianjin Zhongneng Lithium Co. LTD) was used as anode in the cells and the P(IL-PEGDA) solid polymer (80~100 μm) electrolyte was used as solid electrolyte to ensure good interfacial contact. The P(IL-PEGDA) solid polymer electrolyte was prepared by mixing 1-Vinyl-3-butylimidazolium bis-(trifluoromethylsulfonyl)imide (Lanzhou Institute of Chemical Physics), poly(ethylene glycol) diacrylate (Mn = 1000 g mol^{-1}, Aladdin) and LiTFSI (mass ratio = 28:5:12) first, then appropriate amount of anhydrous acetonitrile was added with stirring for 3 h. After that, phenylbis(2,4,6-trimethylbenzoyl)phosphine oxide as a photoinitiator (1 wt% of the monomers) was added in and stirred for 30 min. The mixture was blade-casted onto a glass substrate and photocured by a 365 nm ultraviolet light for 2 min, followed by vacuum-dried at 60 °C overnight to remove the anhydrous acetonitrile, and the P(IL-PEGDA) solid polymer electrolyte was obtained[56]. The cathode electrode slurry was prepared by adding LiFePO$_4$ (KJGROUP), AB (Alfa Aesar), CNTs (2.4 wt% in N-methylpyrrolidone (NMP)), PVDF (Solef 5130) and Li-RCC1-ClO$_4$ with a mass ratio of 71:4:2:3:20 into a mixture of NMP (99.9%, Aladdin) and methyl alcohol (anhydrous, ≥99.9%, Sigma-Aldrich) with a volume ratio of 1:1. The slurry was casted on Al foil (>99.3%, 16 μm, Hefei Kojing Material Technology Co., LTD) and dried at 80 °C for 12 h. To make intimate contact between the different components, the cathode electrode with LiFePO$_4$ areal loading in the range from 1.0 to 4.0 mg cm^{-2} was roll pressed by a roller mill (MSK-HRP-01, Hefei Kojing Material Technology Co., LTD) to densities of 1.24~4.96 g cm^{-3}. The weight ratio of the cathode components without

the Li-RCC1-ClO$_4$ additive is LiFePO$_4$:AB:CNTs:PVDF = 71:4:2:3. While weight ratio of the cathode components with the PEO/LiClO$_4$ additive is LiFePO$_4$:AB:CNTs:PEO/LiClO$_4$ = 71:4:2:23. For the battery coupled with the LLZO pellet (polished to ~300 μm before use), 5 μm P(IL-PEGDA) solid polymer electrolyte[56] was in situ grown on one side of LLZO pellet facing the Li anode, while the cathode slurry was cast on another side of LLZO, then Al foil was covered on the sample before it dried at 80 °C. For the ionic conductivity tests of the solid-state cathodes, the cathode slurry only contains cage electrolyte and LiFePO$_4$ at three different mass ratios (cage electrolyte:LiFePO$_4$ = 10:90, 20:80, and 30:70) was casted on the Al foil with a ~25 μm Au layer; after it was dried and roll-pressed, ~25 μm Au film (diameter of 8 mm) was sputtered on another side of the cathode, then the symmetric cells were assembled in an argon-filled glove box for further tests. For the LCO and NCM523 cathodes, the weight ratio of the cathode components was LCO/NCM523: AB:CNTs:PVDF: Li-RCC1-ClO$_4$ =74:2:1:3:20, the SSE between the cathode and anode can withstand high-voltage (>4.5 V) which is polymerized by 1-allyl-1-methyl- pyrrolidinium Bis (trifluoromethanesulfonyl) imide, 1H,1H,6H,6H-perfluorohexanediyl diacrylate, and vinyl ethylene carbonate. The Li|SPE|LiFePO$_4$ (or LCO/NCM523) batteries were assembled layer by layer and sealed at 50 kg cm^{-2} by a battery sealing machine (MSK-110, Hefei Kojing Material Technology Co., LTD). The electrochemical performance of the batteries was measured on a Neware BTS battery tester in a room with air conditions to control the temperature at 25 ± 3 °C

Data availability

Additional data on methods, materials characterizations and electrochemical performance are available in Supplementary Information. Source data are provided with this paper.

References

1. Sun, C. et al. Recent advances in all-solid-state rechargeable lithium batteries. *Nano Energy* 33, 363–386 (2017).
2. Fan, L. et al. Recent progress of the solid-state electrolytes for high-energy metal-based batteries. *Adv. Energy Mater.* 8, 1702657 (2018).
3. Liu, X., Li, X., Li, H. & Wu, H. B. Recent progress of hybrid solid-state electrolytes for lithium batteries. *Chemistry* 24, 18293–18306 (2018).
4. Zheng, F. et al. Review on solid electrolytes for all-solid-state lithium-ion batteries. *J. Power Sources* 389, 198–213 (2018).
5. Li, J. et al. Covalent interfacial coupling for hybrid solid-state Li ion conductor. *Energy Storage Mater.* 24, 277–283 (2019).
6. Park, K. H. et al. Design strategies, practical considerations, and new solution processes of sulfide solid electrolytes for all-solid-state batteries. *Adv. Energy Mater.* 8, 1800035 (2018).
7. Bucci, G. et al. Mechanical instability of electrode-electrolyte interfaces in solid-state batteries. *Phys. Rev. Mater.* 2, 105407 (2018).
8. Jin, F. et al. High performance solid-state battery with integrated cathode and electrolyte. *Acta Phys. Chim. Sin.* 35, 1399–1403 (2019).
9. Hou, W. et al. Solid electrolytes and interfaces in all-solid-state sodium batteries: progress and perspective. *Nano Energy* 52, 279–291 (2018).
10. Shao, Y. et al. Drawing a soft interface: an effective interfacial modification strategy for garnet-type solid-state Li batteries. *ACS Energy Lett.* 3, 1212–1218 (2018).
11. Shen, Y. et al. Unlocking the energy capabilities of lithium metal electrode with solid-state Electrolytes. *Joule* 2, 1674–1689 (2018).
12. Cheng, X.-B. et al. Recent advances in energy chemistry between solid-state electrolyte and safe lithium-metal anodes. *Chem* 5, 74–96 (2019).
13. Dong, D. et al. Polymer electrolyte glue: a universal interfacial modification strategy for all-solid-state Li batteries. *Nano Lett.* 19, 2343–2349 (2019).
14. Culver, S. P., Koerver, R., Zeier, W. G. & Janek, J. On the functionality of coatings for cathode active materials in thiophosphate-based all-solid-state batteries. *Adv. Energy Mater.* 9, 1900626 (2019).
15. Cao, D. X. et al. Processing strategies to improve cell-level energy density of metal sulfide electrolyte based all-solid-state Li metal batteries and beyond. *ACS Energy Lett.* 5, 3468–3489 (2020).
16. Wang, C. et al. Solid-state plastic crystal electrolytes: effective protection interlayers for sulfide-based all-solid-state lithium metal batteries. *Adv. Funct. Mater.* 29, 1900392 (2019).
17. Gao, H., Xue, L., Xin, S., Park, K. & Goodenough, J. B. A plastic-crystal electrolyte interphase for all-solid-state sodium batteries. *Angew. Chem. Int. Ed.* 56, 5541–5545 (2017).
18. Zhou, D. et al. In situ synthesis of a hierarchical all-solid-state electrolyte based on nitrile materials for high-performance lithium-ion batteries. *Adv. Energy Mater.* 5, 1500353 (2015).

9

19. Chen, S. J. et al. all-solid-state batteries with a limited lithium metal anode at room temperature using a garnet-based electrolyte. *Adv. Mater.* **33**, 2002325 (2021).

20. Kato, Y. et al. High-power all-solid-state batteries using sulfide superionic conductors. *Nat. Energy* **1**, 16030 (2016).

21. Yan, X., Li, Z., Wen, Z. & Han, W. Li/Li$_7$La$_3$Zr$_2$O$_{12}$/LiFePO$_4$ all-solid-state battery with ultrathin nanoscale solid electrolyte. *J. Phys. Chem. C* **121**, 1431–1435 (2017).

22. Kerman, K., Luntz, A., Viswanathan, V., Chiang, Y.-M. & Chen, Z. Review-practical challenges hindering the development of solid state Li ion batteries. *J. Electrochem. Soc.* **164**, A1731–A1744 (2017).

23. Xu, R.-C. et al. All-solid-state lithium–sulfur batteries based on a newly designed Li$_7$P$_{2.9}$Mn$_{0.1}$S$_{10.7}$I$_{0.3}$ superionic conductor. *J. Mater. Chem. A* **5**, 6310–6317 (2017).

24. Lin, D. et al. High ionic conductivity of composite solid polymer electrolyte via in situ synthesis of monodispersed SiO$_2$ nanospheres in poly(ethylene oxide). *Nano Lett.* **16**, 459–465 (2016).

25. Jung, Y. C., Lee, S. M., Choi, J. H., Jang, S. S. & Kim, D. W. All solid-state lithium batteries assembled with hybrid solid electrolytes. *J. Electrochem. Soc.* **162**, A704–A710 (2015).

26. Ma, C. et al. High ion-conducting solid-state composite electrolytes with carbon quantum dot nanofillers. *Adv. Sci.* **5**, 1700996 (2018).

27. Chen, R. S. et al. Approaching practically accessible solid-state batteries: stability issues related to solid electrolytes and interfaces. *Chem. Rev.* **120**, 6820–6877 (2020).

28. Yamada, T. et al. All solid-state lithium-sulfur battery using a glass-type P$_2$S$_5$-Li$_2$S electrolyte: benefits on anode kinetics. *J. Electrochem. Soc.* **162**, A646 (2015).

29. Han, F. et al. Interphase engineering enabled all-ceramic lithium battery. *Joule* **2**, 497–508 (2018).

30. Rosero-Navarro, N. C., Miura, A. & Tadanaga, K. Composite cathode prepared by argyrodite precursor solution assisted by dispersant agents for bulk-type all-solid-state batteries. *J. Power Sources* **396**, 33–40 (2018).

31. Wiers, B. M. et al. A solid lithium electrolyte via addition of lithium isopropoxide to a metal-organic framework with open metal sites. *J. Am. Chem. Soc.* **133**, 14522–14525 (2011).

32. Horike, S., Umeyama, D. & Kitagawa, S. Ion conductivity and transport by porous coordination polymers and metal-organic frameworks. *Acc. Chem. Res.* **46**, 2376–2384 (2013).

33. Jeong, K. et al. Solvent-free, single lithium-ion conducting covalent organic frameworks. *J. Am. Chem. Soc.* **141**, 5880–5885 (2019).

34. Demetrius, A. et al. Mechanically shaped two-dimensional covalent organic frameworks reveal crystallographic alignment and fast Li-ion conductivity. *J. Am. Chem. Soc.* **138**, 9767–9770 (2016).

35. Chen, H. et al. Cationic covalent organic framework nanosheets for fast Li-ion conduction. *J. Am. Chem. Soc.* **140**, 896–899 (2018).

36. Tozawa, T. et al. Porous organic cages. *Nat. Mater.* **8**, 973–978 (2009).

37. Hasell, T. & Cooper, A. I. Porous organic cages: soluble, modular and molecular pores. *Nat. Rev. Mater.* **1**, 16053 (2016).

38. Petronico, A. et al. Solid-liquid lithium electrolyte nanocomposites derived from porous molecular cages. *J. Am. Chem. Soc.* **140**, 7504–7509 (2018).

39. Park, J. H. et al. Solid lithium electrolytes based on an organic molecular porous solid. *Chem. Commun.* **51**, 9313–9316 (2015).

40. Wang, Z. F. et al. Soft porous crystal based upon organic cages that exhibit guest induced breathing and selective gas separation. *J. Am. Chem. Soc.* **141**, 9408–9414 (2019).

41. Liu, M. et al. Three-dimensional protonic conductivity in porous organic cage solids. *Nat. Commun.*, **7**, 12750 (2016).

42. Swamy, S. I. et al. A metal-organic framework with a covalently prefabricated porous organic linker. *J. Am. Chem. Soc.* **132**, 12773–12775 (2010).

43. Pandey, G. P. & Rastogi, A. C. Pulse polymerized poly(3,4-ethylenedioxythiophene) electrodes for solid-state supercapacitors with ionic liquid gel polymer electrolyte. *Mater. Res. Soc.* **1448** (2012).

44. Süzer, Ş., Birer, Ö. Sevil, U. A., Güven, O. XPS investigations on conducting polymers. *Tr. J. Chem.* **22**, 59–66 (1998).

45. Spanninga, S. A., Martin, D. C. & Chen, Z. X-ray photoelectron spectroscopy study of counterion incorporation in Poly(3,4-ethylenedioxythiophene). *J. Phys. Chem. C.* **113**, 5585–5592 (2009).

46. Schantz, S. On the ion association at low salt concentrations in polymer electrolytes; a Raman study of NaCF$_3$SO$_3$ and LiClO$_4$ dissolved in poly(propylene oxide). *J. Chem. Phys.* **94**, 6296–6306 (1991).

47. Ostrovskii, D. et al. Molecular and ionic interactions in poly(acrylonitrile)-and poly(methylmetacrylate)-based gel electrolytes. *J. Chem. Phys.* **109**, 7618–7624 (1998).

48. Terashima, Y., Takeda, K. & Honda, M. Raman and density functional theory studies of solvation structure and ion association of NaClO$_4$ in 1,2-propanediamine. *Chem. Phys.* **430**, 23–28 (2014).

49. Quartarone, E., Mustarelli, P. & Magistris, A. J. S. S. I. PEO-based composite polymer electrolytes. *Solid State Ion.* **110**, 1–14 (1998).

50. Ma, Y. et al. Effect of montmorillonite on the ionic conductivity and electrochemical properties of a composite solid polymer electrolyte based on polyvinylidenedifluoride/polyvinyl alcohol matrix for lithium ion batteries. *Electrochim. Acta* **187**, 535–542 (2016).

51. Zhang, H. et al. Lithium bis (fluorosulfonyl) imide/poly (ethylene oxide) polymer electrolyte. *Electrochim. Acta* **133**, 529–538 (2014).

52. Puthirath, A. B. et al. Transparent flexible lithium ion conducting solid polymer electrolyte. *J. Mater. Chem. A* **5**, 11152–11162 (2017).

53. Borodin, O. & Smith, G. D. Mechanism of ion transport in amorphous poly(ethylene oxide)/LiTFSI from molecular dynamics simulations. *Macromol* **39**, 1620–1629 (2006).

54. Jeong, K., Park, S. & Lee, S. Y. Revisiting polymeric single lithium-ion conductors as an organic route for all-solid-state lithium ion and metal batteries. *J. Mater. Chem. A.* **7**, 1917 (2019).

55. Jinisha, B. et al. Development of a novel type of solid polymer electrolyte for solid state lithium battery applications based on lithium enriched poly (ethylene oxide)(PEO)/poly (vinyl pyrrolidone)(PVP) blend polymer. *Electrochim. Acta* **235**, 210–222 (2017).

56. Zhang, F. R. et al. Highly conductive polymeric ionic liquid electrolytes for ambient temperature solid-state lithium batteries. *ACS Appl. Mater. Interfaces* **12**, 23774–23780 (2020).

57. Aguilo-Aguayo, N. et al. Water-based slurries for high-energy LiFePO$_4$ batteries using embroidered current collectors. *Sci. Rep.* **10**, 5565–5565 (2020).

58. Cheng, S. H.-S. et al. Electrochemical performance of all-solid-state lithium batteries using inorganic lithium garnets particulate reinforced PEO/LiClO$_4$ electrolyte. *Electrochim. Acta* **253**, 430–438 (2017).

59. Lee, Y. G. et al. High-energy long-cycling all-solid-state lithium metal batteries enabled by silver–carbon composite anodes. *Nat. Energy* **5**, 299–308 (2020).

60. Kasemchainan, J. et al. Critical stripping current leads to dendrite formation on plating in lithium anode solid electrolyte cells. *Nat. Mater.* **18**, 1105–1111 (2019).

61. Yang, L. et al. Flexible composite solid electrolyte facilitating highly stable "soft contacting" Li-electrolyte interface for solid state lithium-ion batteries. *Adv. Energy Mater.* **7**, 1701437 (2017).

62. Yuan, X. F. et al. A polyoxometalate-based polymer electrolyte with an improved electrode interface and ion conductivity for high-safety all-solid-state batteries. *J. Mater. Chem. A* **7**, 15924 (2019).

63. Wu, J. F. & Guo, X. Nanostructured metal–organic framework (MOF)-derived solid electrolytes realizing fast lithium ion transportation kinetics in solid-state batteries. *Small* **15**, 1804413 (2019).

64. Wan, J. et al. Ultrathin, flexible, solid polymer composite electrolyte enabled with aligned nanoporous host for lithium batteries. *Nat. Nanotechnol.* **14**, 705–711 (2019).

65. Li, Y. et al. Mastering the interface for advanced all-solid-state lithium rechargeable batteries. *PNAS* **22**, 13313–13317 (2016).

66. Chen, S. et al. In-situ preparation of poly(ethylene oxide)/Li$_3$PS$_4$ hybrid polymer electrolyte with good nanofiller distribution for rechargeable solid-state lithium batteries. *J. Power Sources* **387**, 72–80 (2018).

67. Randau, S. et al. Benchmarking the performance of all-solid-statelithium batteries. *Nat. Energy* **5**, 259–270 (2020).

68. Kang, Tuo et al. Self-assembled monolayer enables slurry-coating of Li anode. *ACS Cent. Sci.* **5**, 468–476 (2019).

Acknowledgements

Author contributions

L.C. conceived the original idea. M.L., A.I.C. and L.C. participated in the initial discussion of the project. J.L., H.C., Y.Q., Y.S. and L.C. designed the details of the experiments. J.L., J.Q., F.J., F.Z. and L.T. prepared the samples. J.L., J.Q., and J.X. performed the electrochemical tests. J.L., L.Z., and R.H. carried out the XPS and TOF-SIMS characterization. J.L., Y.Q., Y.S., M.L., A.I.C. and L.C. wrote the paper. All authors were involved in analysis of the experimental data, discussion of the results, and the preparation of the manuscript.

Competing interests

The authors declare no competing interests.

Additional information

Supplementary information The online version contains supplementary material available at https://doi.org/10.1038/s41467-022-29743-1.

Correspondence and requests for materials should be addressed to Yejun Qiu, Andrew I. Cooper, Yanbin Shen or Liwei Chen.

Peer review information *Nature Communications* thanks the anonymous reviewer(s) for their contribution to the peer review of this work.

Reprints and permission information is available at http://www.nature.com/reprints

Publisher's note Springer Nature remains neutral with regard to jurisdictional claims in published maps and institutional affiliations.